



On-demand multimode optical storage in a laser-written on-chip waveguide

Ming-Xu Su, Tian-Xiang Zhu, Chao Liu, Zong-Quan Zhou ^{*}, Chuan-Feng Li [†] and Guang-Can Guo
CAS Key Laboratory of Quantum Information, University of Science and Technology of China, Hefei 230026, China;
CAS Center for Excellence in Quantum Information and Quantum Physics, University of Science
and Technology of China, Hefei 230026, China
and Hefei National Laboratory, University of Science and Technology of China, Hefei 230088, China



(Received 12 August 2021; revised 26 March 2022; accepted 11 May 2022; published 23 May 2022)

Quantum memory is a fundamental building block for large-scale quantum networks. On-demand optical storage with a large bandwidth, a high multimode capacity, and an integrated structure simultaneously is crucial for practical application. However, this has not been demonstrated yet. Here, we fabricate an on-chip waveguide in a $^{151}\text{Eu}^{3+}:\text{Y}_2\text{SiO}_5$ crystal with insertion losses of 0.2 dB, and propose a pumping scheme to enable spin-wave atomic frequency comb (AFC) storage with a bandwidth of 11 MHz inside the waveguide. Based on this, we demonstrate the storage of 200 temporal modes using the AFC scheme and conditional on-demand storage of 100 temporal modes using the spin-wave AFC scheme. The interference visibility between the readout light field and the reference light field is $99.0\% \pm 0.6\%$ and $97\% \pm 3\%$ for AFC and spin-wave AFC storage, respectively, indicating the coherent nature of this low-loss, multimode, and integrated storage device.

DOI: [10.1103/PhysRevA.105.052432](https://doi.org/10.1103/PhysRevA.105.052432)

I. INTRODUCTION

As an interface between light and matter, optical quantum memories (QMs) are of vital importance in quantum information science [1,2]. Rare-earth-ion (REI) doped crystals are promising candidates for quantum memories because of the long-lived coherence for both the optical transition [3] and the hyperfine transition [4], and the large bandwidth [5], which enables a high multimode capacity.

Multimode storage is a key tool to enhance the data rate of memory-based quantum communication [6]. Recently, this property is demonstrated in an elementary quantum repeater segment based on multimode quantum memories [7,8]. The temporal multimode capacity is determined by the time-bandwidth product (storage time \times bandwidth) of a memory. For Kramers ions, such as Nd^{3+} , Er^{3+} , and Yb^{3+} , a large storage bandwidth can be obtained due to the large hyperfine splittings. Quantum storage of 100 single photons with a predetermined storage time was demonstrated with $\text{Nd}^{3+}:\text{YVO}_4$ [9] and storage of 1060 classical light pulses was demonstrated with $\text{Tm}^{3+}:\text{YAG}$ [10]. However, on-demand spin-wave storage is challenging due to the superhyperfine interactions and fast spin dephasing of these materials. This difficulty was recently overcome by using the zero-field zero first-order Zeema point. On-demand single-mode storage with a bandwidth of 10 MHz is demonstrated with $\text{Yb}^{3+}:\text{Y}_2\text{SiO}_5$ [11]. For non-Kramers ions, such as Eu^{3+} and Pr^{3+} , the nuclear spin states provide long storage time while the bandwidth is typically limited to 10 MHz [12–15]. $^{151}\text{Eu}^{3+}:\text{Y}_2\text{SiO}_5$ is a unique material that has enabled optical storage for 1 h [16] and has

the longest spin coherence time among all matter systems [4]. On-demand optical storage of 50 temporal modes has been demonstrated in this material with a storage bandwidth of 5 MHz [17].

Integrated optical QMs are required in order to connect with other integrated devices and to build the quantum network with integrated architectures. Many techniques have been used to fabricate integrated optical memories based on REI doped crystals, such as femtosecond laser micromachining (FLM) [18–23], focused-ion-beam milling [24–26], Ti diffusion in LiNbO_3 waveguide [5,27–31], and optical fibers [32,33]. FLM has the advantages of low damage to the substrate and three-dimensional fabrication capability [34]. Multimode quantum storage of 15 frequency modes and nine temporal modes with a predetermined storage time has been demonstrated in a laser-written type-I waveguide based on $\text{Pr}^{3+}:\text{Y}_2\text{SiO}_5$ [20]. Recently, our group demonstrated the on-demand qubit storage in a type-IV on-chip waveguide fabricated on $\text{Eu}^{3+}:\text{Y}_2\text{SiO}_5$ [23].

Here, we fabricate a low-loss type-II waveguide close to the surface of a $^{151}\text{Eu}^{3+}:\text{Y}_2\text{SiO}_5$ crystal. We demonstrate on-demand optical storage with a bandwidth of 11 MHz and a multimode capacity of 100. The reliability of this device is confirmed by the high interference visibility ($99.0\% \pm 0.6\%$ for AFC and $97\% \pm 3\%$ for spin-wave AFC) between the readout light field and the reference light field.

II. FABRICATION OF THE WAVEGUIDE

The substrate is a 0.1% doped $^{151}\text{Eu}^{3+}:\text{Y}_2\text{SiO}_5$ crystal, with a dimension of $15 \times 4 \times 3$ mm ($b \times D_1 \times D_2$) and an isotopic enrichment of 99% for $^{151}\text{Eu}^{3+}$. The configuration of the FLM waveguide is defined as four types according to the relative position of the tracks and reflective-index changes

^{*}zq_zhou@ustc.edu.cn

[†]cfl@ustc.edu.cn

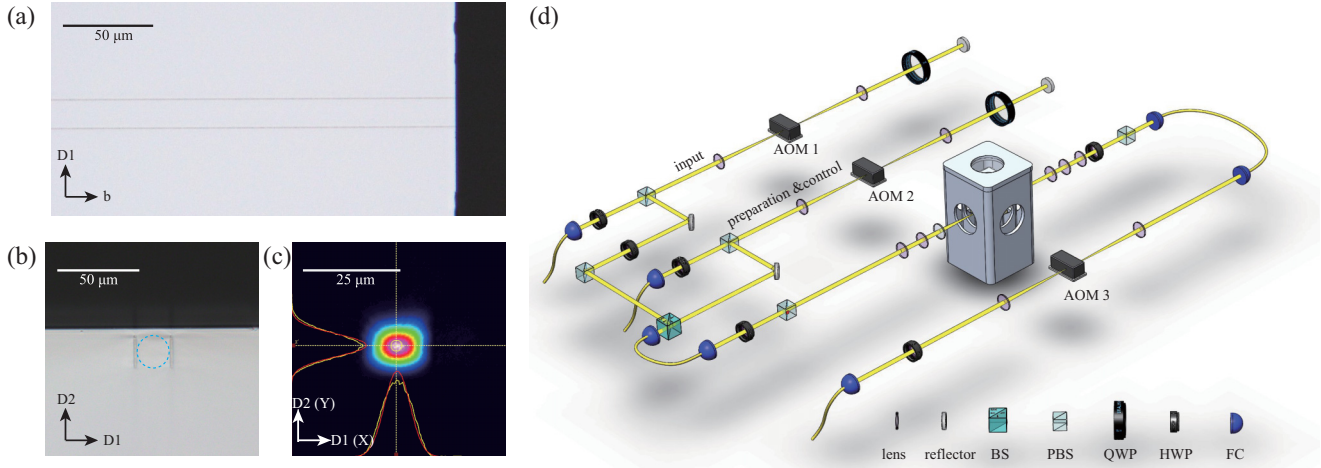


FIG. 1. (a) The top view of the type-II waveguide under an optical microscope. (b) The side view of the type-II waveguide under an optical microscope. The blue dashed ellipse indicates the guided regime. (c) The intensity profile of guided mode as measured at the exit surface of the waveguide. The full width at half maximum of the guided mode is measured as $\Delta_x = 7.6 \mu\text{m}$ and $\Delta_y = 7.1 \mu\text{m}$. The red lines show the Gaussian fits. (d) Experimental setup. The acoustic optical modulator (AOM) 1 and the AOM 2 are in double-pass configurations. The input beam and the preparation and control beam are combined by a beam splitter then coupled into the waveguide. The AOM 3 is in single-pass configuration and serves as a temporal gate. The output beam from AOM 3 was collected by a fiber coupler and sent into a photodetector. Labels at the right corner are as follows: BS, beam splitter; PBS, polarizing beam splitter; QWP, quarter-wave plate; HWP, half-wave plate; and FC, fiber coupler.

introduced by the femtosecond laser [34]. Here we fabricated a type-II waveguide very close to the substrate's surface, which enables the interface with other on-chip integrated devices. The type-II waveguide is fabricated by a FLM system from WOPhotonics (Altechna R&D Ltd, Lithuania). The femtosecond laser with a wavelength of 1030 nm is injected on the crystal along the D_2 axis through a microscope objective ($50\times$, 0.65 NA). In order to minimize transmission loss, the laser parameters are optimized as follows: pulse duration of 210 fs, energy per pulse of 64 nJ, repetition rate of 201.9 kHz, polarization along the b axis, and sample movement speed along the b axis of 1 mm/s. Note that the energy per pulse of 64 nJ is much smaller than that used in our previous work [21], which results in smoother sidewalls and lower losses. The resulted damage track is $7 \mu\text{m}$ along the femtosecond laser propagation direction (D_2 axis). To match the mode of input Gaussian beam, a waveguide with a height and a width of $21 \mu\text{m}$ is fabricated. Each edge is formed by three tracks with a depth increment of $7 \mu\text{m}$. After this, a single-mode waveguide for 580-nm laser is fabricated near the surface of the crystal (see Fig. 1). The femtosecond laser causes a decrease of refractive index in the irradiated regions, so the 580-nm laser polarized along the D_1 axis is bounded in the waveguide region, while the laser polarized along the D_2 axis cannot be confined. After the fabrication, the crystal is annealed in air at 800°C for 4 h and cooled to room temperature in 8 h. This annealing process reduces the insertion loss (calculated as the ratio of transmission of the waveguide regime and that of the bulk regime of the same crystal; see more details in Appendix A) of the waveguide from 0.4 to 0.2 dB. The full width at half maximum (FWHM) of the guided mode is measured as $\Delta_x = 7.6 \mu\text{m}$ and $\Delta_y = 7.1 \mu\text{m}$ (X represents the direction along the D_1 axis, Y represents the direction along the D_2 axis) [Fig. 1(c)]. After the fabrication process, we

measured the coherence time T_2 using two-pulse photon echo experiments. The optical coherence lifetime T_2 of the excited state is measured as $241 \mu\text{s}$ for waveguide regime with a peak power of the input pulse of 0.13 mW. For comparison, the optical coherence lifetime T_2 in bulk regime is $267 \mu\text{s}$ with a peak power of the input pulse of 0.98 mW. These results indicate that the waveguide fabrication process does not affect the coherence property of the sample.

III. EXPERIMENTAL SETUP

A frequency-doubled semiconductor laser (TA-SHG, Topptica) serves as the laser source, which is stabilized to a high-finesse Fabry-Perot cavity at the frequency of 516.849 THz with a linewidth of sub-kHz. The $^{151}\text{Eu}^{3+}:\text{Y}_2\text{SiO}_5$ crystal is cooled to approximately 3.1 K in a closed-cycle cryostat (Montana Instrument) and mounted on a three-axis translation stage to facilitate the waveguide coupling. The laser is modulated by the acoustic optical modulators (AOMs) driven by an arbitrary waveform generator. As shown in Fig. 1(d), the signal beam is generated by AOM 1, which can control the phase and the amplitude of the input pulse. The AOM 2 is employed to generate the preparation and control beam. Those two beams are combined by a 90:10 beam splitter and coupled into the waveguide by three lenses. By adjusting those three lenses, beam diameter is adjusted to match the mode of the waveguide (see Appendix A). A fiber coupler collects the output beam into a single-mode fiber. The output pulses is finally detected by a photodetector after passing a temporal gate based on the AOM 3. The overall transmission efficiency from the front of the cryostat to the single-mode fiber is 56%. Since the main loss is due to the reflections of the uncoated sample surfaces and other optical elements, higher efficiencies can be obtained with better antireflection coatings.

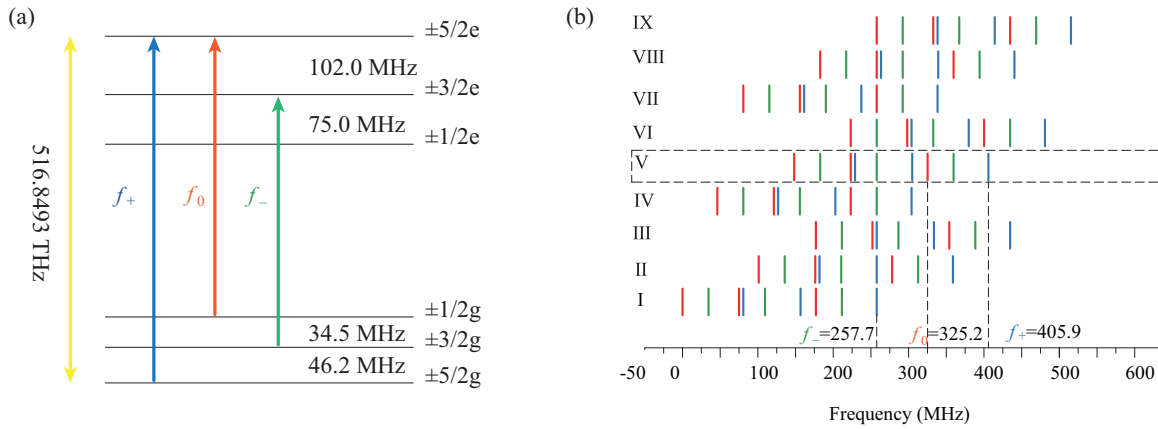


FIG. 2. (a) The energy level diagram of the ${}^7F_0 \rightarrow {}^5D_0$ transition of ${}^{151}\text{Eu}^{3+}$ in Y_2SiO_5 crystal. The input pulses with the center frequency of f_0 are resonant with $|\pm 1/2\rangle_g \rightarrow |\pm 5/2\rangle_e$, and the control pulses with the center frequency of f_+ are resonant with $|\pm 5/2\rangle_g \rightarrow |\pm 5/2\rangle_e$. Pulses with the center frequency of f_- are necessary in the spectral preparation process. (b) Stick diagram of all 81 transitions for ions of class I–IX. The red sticks represent the transitions from $|\pm 1/2\rangle_g$. The green sticks represent the transitions from $|\pm 3/2\rangle_g$. The blue sticks represent the transitions from $|\pm 5/2\rangle_g$. The relative frequency of each transition can be calculated from the energy level diagram (see Appendix B). Ions of class V are selected for the experiment. The maximum bandwidth of 11.7 MHz is limited to the gap (11.7 MHz) between the third green stick of class-VIII ions and the third blue stick of class-V ions.

IV. RESULTS

A. The preparation of an 11-MHz Λ system in ${}^{151}\text{Eu}^{3+}:\text{Y}_2\text{SiO}_5$

The atomic frequency comb (AFC) is an established protocol for spin-wave quantum storage in REI doped solids [13–15]. Spectral-hole burning is employed to prepare a comb-like absorption structure (with a periodicity of Δ) in the inhomogeneously broadened optical transition [12,35]. Input pulse absorbed by this structure will dephase and rephase, leading to a photon-echo-like emission at time $1/\Delta$ [36]. In order to achieve on-demand and long-lived storage, the spin-wave AFC scheme can be implemented, which requires applying a pair of control pulses before the two-level AFC echo appears. The first control pulse is applied to map the excitation into the spin state. After the time T_s , the second control pulse brings it back and continue the AFC rephasing. The total storage time $T = 1/\Delta + T_s$.

The multimode capacity in the time domain of the AFC scheme is proportional to the number of comb teeth [36], which depends on the total bandwidth and the periodicity Δ . While for spin-wave AFC memory, the storage bandwidth will be further limited by hyperfine splittings, depending the chosen Λ system. So far, this bandwidth is limited to 5 MHz in ${}^{151}\text{Eu}^{3+}:\text{Y}_2\text{SiO}_5$ [13,14,17,21,22]. In order to overcome this limitation, we choose a different Λ system from previous works, which has a larger bandwidth of 11 MHz but a lower transition probability [35] for the control pulses. However, the manipulation of such weak transition can be achieved inside a waveguide due to the strong confinement of light in the small interaction area.

The inhomogeneous broadening of ${}^7F_0 \rightarrow {}^5D_0$ transition is approximately 3 GHz, which is much larger than the hyperfine splitting (Fig. 2). Nine classes of ions will interact with the input laser [Fig. 2(b)]. To implement spin-wave AFC scheme, optical pumping is required to isolate a Λ system involving a single class of ions [13]. To maximize the useful bandwidth of the Λ system, we design a strategy for

optical pumping. Setting the frequency of transition $|\pm 1/2\rangle_g \rightarrow |\pm 1/2\rangle_e$ as zero, those transitions with the frequency of $f_- = 257.7$ MHz, $f_0 = 325.2$ MHz, and $f_+ = 405.9$ MHz are shown in Fig. 2(b). The first step is to simultaneously apply two 20-MHz sweeping pulses with center frequencies of f_0 and f_+ to pump all populations into the ground state $|\pm 3/2\rangle_g$ and create two transparent pits in $|\pm 1/2\rangle_g$ and $|\pm 5/2\rangle_g$. The second step is applying 11-MHz sweeping pulses with the center frequency of f_- , to pump back ions into the pit in $|\pm 1/2\rangle_g$. Meanwhile, 11-MHz sweeping pulses with the center frequency of f_+ are applied to clean the $|\pm 5/2\rangle_g$. After those preparation sequences, ions of class V are selected. The bandwidth is limited to 11.7 MHz because the transition $|\pm 3/2\rangle_g \rightarrow |\pm 5/2\rangle_e$ of class-VIII ions will mix with the $|\pm 5/2\rangle_g$ of class-V ions [Fig. 2(b)]. In the first two steps, each pulse has a duration of 1 ms and repeats 10 times. The third step is to create the comb on $|\pm 1/2\rangle_g \rightarrow |\pm 5/2\rangle_e$ by using the parallel preparation sequences [17]. The preparation pulse has a duration time of 5 ms and repeats 76 times. An 11-MHz sweeping pulse with the center frequency of f_+ is applied after every two preparation pulses to keep the $|\pm 5/2\rangle_g$ empty. Finally, the AFC with a bandwidth of 11 MHz and a periodicity of 20 kHz is created with the measured structure presented in Fig. 3.

B. The multimode AFC storage

Here, we perform a multimode AFC storage of 200 temporal modes with low cross talk. As shown in Fig. 4, 200 temporal modes are injected and each input mode has a mode size of 200 ns and a full width at half maximum (FWHM) of approximately 70 ns, which matches the bandwidth of 11 MHz. After $1/\Delta = 50 \mu\text{s}$, AFC echoes appear. Each AFC echo has a FWHM of approximately 73 ns and a mode size of approximately 200 ns, which indicates that nearly all of the input mode is stored. The AFC efficiency is defined as the ratio between the intensity of the AFC echo and the input

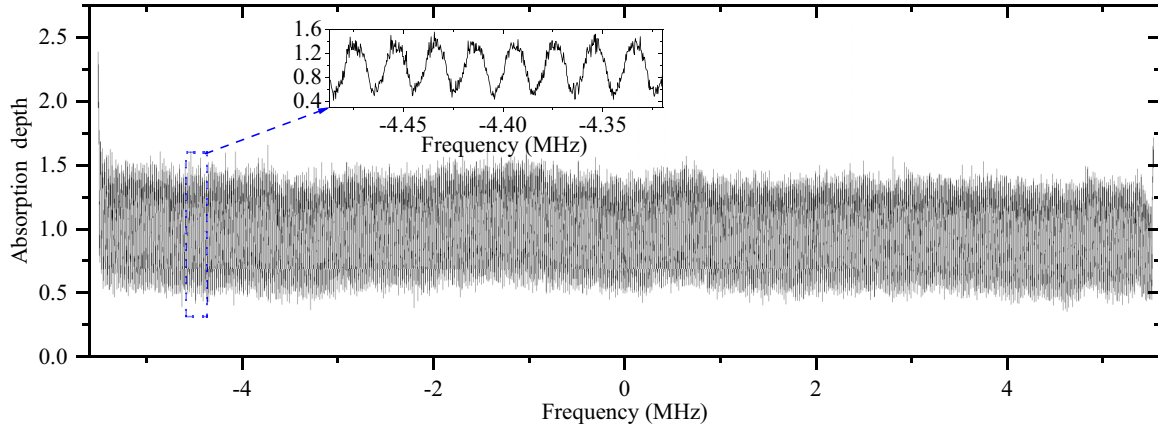


FIG. 3. The measured AFC structure with a bandwidth of 11 MHz and periodicity of 20 kHz. The frequency is represented by the detuning to f_0 . There are 550 teeth in total. The peak absorption and background absorption is approximately 1.05 and 0.44 respectively. The finesse is approximately 2.3. The inset shows the details of the AFC structure.

pulse. The retrieved AFC echoes have an average efficiency of $2.5\% \pm 0.2\%$. This value agrees with the theoretical storage efficiency of 2.3% estimated from the AFC structure by using the formula $\eta = e^{-\tilde{d}} \tilde{d}^2 e^{-7/F^2} e^{-d_0}$ [1]. Here, $\tilde{d} = d/F$, where d is the peak absorption depth, d_0 is the background absorption depth, and F is the finesse of the AFC, and these parameters are provided in Fig. 3. Assuming $d = 1.49$ and a background absorption $d_0 = 0$, the highest theoretical efficiency of 11.3% can be predicted with a square-shaped comb peak with a finesse of 2.35 [36,37]. The reduced efficiency in our experiment is due to the imperfect pumping caused by some technical issues (finite laser linewidth, vibration of the cryostat), which can be especially significant for AFC with large bandwidth and long storage times.

To verify the coherent nature of this highly multimode memory, 200 synchronized reference pulses are injected into

the waveguide along the same path as the input signal pulses. The phase of each pulse is increased by 4 deg, one by one, while the phase of all input pulses are the same. The interference of the echo and reference pulses form a trigonometric-function-like pattern [Fig. 5(a)], showing that the coherence is well preserved over all modes. Because it is hard to tune every reference pulse to be exactly the same as every echo, there are some remaining signals in the location with a destructive interference.

For more precise measurement, the interference visibility is further measured by operating with only a single mode to precisely tune the mode to overlap between the echo and the reference pulse [Fig. 5(b)]. The reference pulse is tuned to the same shape and same time as the echo but different in phase.

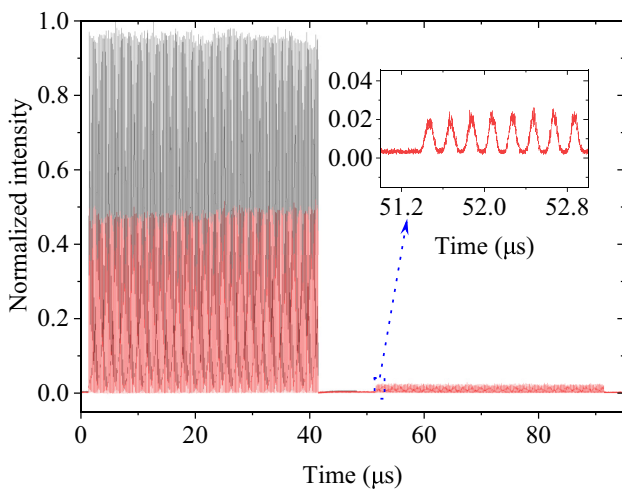


FIG. 4. AFC storage of 200 temporal modes. Each input pulse (black line) has a mode size of 200 ns, matching the AFC bandwidth. The red line shows the trace for AFC storage with a storage time of 50 μs . The average storage efficiency over 200 modes is $2.5\% \pm 0.2\%$. The inset shows the details about the first eight modes after storage.

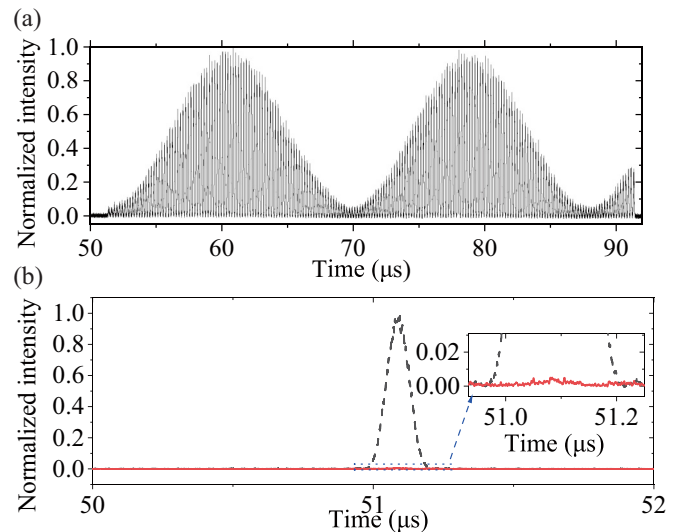


FIG. 5. (a) Interference between 200 echoes and 200 reference pulses in AFC storage. The phase of each reference pulse increases by 4 deg. (b) The traces of the readout echo in the situations of the constructive interference (black dashed line) and the destructive interference (red solid line) which are averaged by ten measurements. The interference visibility is $99.0\% \pm 0.6\%$. The inset shows the details about the destructive interference.

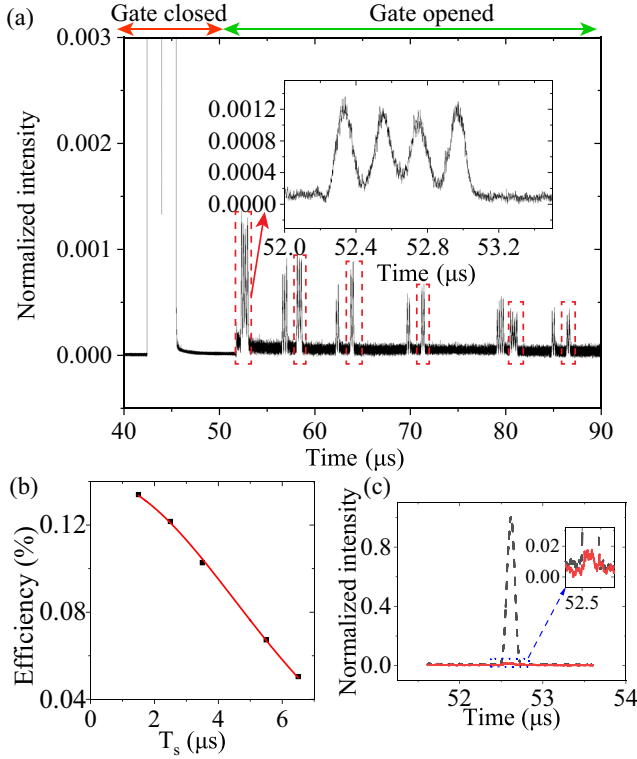


FIG. 6. (a) Spin-wave AFC storage of 100 modes for 51.5 μs . The AOM gate is opened when the spin-wave AFC echoes emit. The peaks in red dashed line are the spin-wave AFC echoes. Other peaks are the remaining part of the AFC echoes. The inset shows the details about the first four modes. (b) The spin-wave AFC efficiency as a function of spin-wave storage time (T_s). The red solid line is a Gaussian function fit with the fitted inhomogeneous spin linewidth of 58.8 ± 0.5 kHz. (c) The traces of spin-wave echo in the situation of the constructive interference (black dashed line) and the destructive interference (red solid line) averaged by ten measurements. The visibility is $97\% \pm 3\%$. The inset shows the details about the destructive interference.

The interference visibility is calculated from $V = \frac{\max - \min}{\max + \min}$, where max and min correspond to the constructive interference intensity and the destructive interference intensity. The visibility is measured to be $V = 99.0\% \pm 0.6\%$.

C. The multimode spin-wave AFC storage

Finally, we demonstrate the temporal multimode memory based on the spin-wave AFC scheme. Compared to the AFC scheme, spin-wave AFC scheme could enable on-demand and long-lived storage. After the AFC is prepared, we inject occupied and empty temporal modes into the waveguide. Then, two control pulses are applied before the AFC echo appears. The control pulses have a power of 140 mW, a chirp bandwidth of 11 MHz and a duration time of 1.5 μs . We demonstrate the conditional on-demand storage of 100 temporal modes with a storage time of 51.5 μs (Fig. 6). The spin-wave AFC echo has a FWHM of approximately 96 ns. The average efficiency of the first four modes is $0.13\% \pm 0.01\%$, which is calculated as the ratio between the intensity of the spin-wave AFC echo and the input pulse.

Assuming the spin broadening as a Gaussian disruption, the efficiency can be written as the formula $\eta(T_s)_{\text{SW}} = \eta(0)_{\text{SW}} \times \exp[-\frac{(\gamma_{\text{inh}} T_s)^2}{2 \ln 2 / \pi^2}]$, where γ_{inh} represents the inhomogeneous spin linewidth [38,39]. By changing the time interval T_s of the two control pulses and recording the amplitude of the output echo, γ_{inh} is determined as 58.8 ± 0.5 kHz [see Fig. 6(b)]. A previous work [40] measured the inhomogeneous broadening is 21 kHz for transition $|\pm 1/2\rangle_g \leftrightarrow |\pm 3/2\rangle_g$ in a bulk crystal. The spin Hamiltonian can be written as $H = D[I_z^2 - \frac{I(I+1)}{3}]$, where D represents a parameter corresponds to the distribution of crystal-field [40,41]. The transition energies can be calculated as $2D$ and $6D$ for $I_z = |\pm 1/2\rangle_g \leftrightarrow |\pm 3/2\rangle_g$ and $I_z = |\pm 1/2\rangle_g \leftrightarrow |\pm 5/2\rangle_g$, respectively. Since the inhomogeneous broadening is proportional to the transition energy, we can estimate the inhomogeneous broadening of transition $|\pm 1/2\rangle_g \leftrightarrow |\pm 5/2\rangle_g$ is 63 kHz, three times that of transition $|\pm 1/2\rangle_g \leftrightarrow |\pm 3/2\rangle_g$. This value agrees with measured $\gamma_{\text{inh}} = 58.8 \pm 0.5$ kHz in our experiment, which indicates that the waveguide fabrication process does not affect the spin inhomogeneous broadening. Using the formula $T_2^* = \frac{\sqrt{2 \ln 2}}{\pi \gamma_{\text{inh}}}$, T_2^* is deduced as 6.4 ± 0.1 μs . The transfer efficiency of each control pulse can be calculated from the formula $\eta_{\text{T}} = \eta_{\text{AFC}} \eta_{\text{T}}^2$ [12]. The efficiency without spin dephasing $\eta_{\text{SW}} = 0.14\%$ can be deduced from Fig. 6(b). The AFC efficiency $\eta_{\text{AFC}} = 2.5\%$. Therefore, the spin transfer efficiency $\eta_{\text{T}} = 23.7\%$. Note that increasing the duration of control pulse can improve the transfer efficiency, but due to the limitation of T_2^* , the storage efficiency will also be attenuated. The 1.5- μs duration time of control pulses is optimized by the spin-wave AFC efficiency. One primary reason for the low spin transfer efficiency is the low oscillator strength of the chosen transition. Nevertheless, our result indicates the advantages of employing the waveguide structure since such experiment performed with the bulk material would require an unrealistic laser power of the control pulse (>10 W). Waveguides with smaller guided mode (such as type-I waveguides [19,20]) may help improve the spin-wave storage efficiency.

Because of the imperfect control pulses, the two-level AFC echoes are not completely suppressed, leading to a conditional on-demand storage of 100 temporal modes. There must be a time delay (the spin-wave storage time) after several input modes are continuously injected to avoid the circumstance that the remaining AFC echoes overlap with the spin-wave AFC echoes. For example, given the spin-wave storage time of 1.5 μs here, no more than seven (the spin-wave storage time of 1.5 μs /the mode size of 200 ns) occupied modes can be actually stored. After that time delay, there is still time to inject the remaining modes in groups of no more than seven modes. The multimode capacity of spin-wave storage is currently limited by the fast spin dephasing. Unconditional spin-wave storage of 200 modes can be obtained by employing the dynamical decoupling to overcome the spin dephasing [16,42]. Since our on-chip waveguide can be easily combined with on-chip coplanar electrical waveguide [26], fast and efficient spin manipulations could be expected. We also notice that the efficiency decreases with the number of modes, similar to that observed in a previous work [17]. This phenomenon still remains to be studied. We further implement a single-mode storage experiment to benchmark the coherent

storage capacity similar as that reported in the previous section. The interference visibility after spin-wave AFC storage is $97\% \pm 3\%$ [Fig. 6(c)], which further reveals that the coherent phase is preserved in the spin-wave AFC storage process.

V. DISCUSSION AND CONCLUSION

An on-chip waveguide with a low insertion loss of 0.2 dB is fabricated on a $^{151}\text{Eu}^{3+}:\text{Y}_2\text{SiO}_5$ crystal using FLM. We extend the storage bandwidth of the $^{151}\text{Eu}^{3+}$ ions to 11 MHz by applying an unusual pumping scheme. Based on this, we demonstrate the 200-mode storage using AFC scheme and conditional 100-mode on-demand storage using the spin-wave AFC scheme. The coherent phases of the stored modes are well preserved during the storage processes. Longer storage times could be obtained by combing with on-chip electrical waveguides to accomplish dynamical decoupling to protect the spin coherence. The storage efficiency is currently limited by the low effective absorption of the sample and the low spin-wave transfer efficiency. Higher AFC efficiencies could be obtained with optimized comb structure and an impedance-matched cavity [43]. Higher spin-wave transfer efficiencies could be obtained by fabricating a waveguide with a smaller guided mode and introducing dynamical decoupling to overcome the spin dephasing. Even without spin-wave storage, the two-level AFC storage with a large multimode capacity can still be useful in nonhierarchical quantum repeaters [30]. The multimode integrated memory demonstrated here could be an important ingredient for the construction of quantum repeater [2,6–8] and transportable quantum memory [4,16], toward the ultimate goal of global-scale quantum communication.

ACKNOWLEDGMENTS

This work is supported by the National Key R&D Program of China (Grant No. 2017YFA0304100), Innovation Program for Quantum Science and Technology (Grant No. 2021ZD0301200), the National Natural Science Foundation of China (Grants No. 11774331, No. 11774335, No. 11821404, and No. 11654002) and the Fundamental Research Funds for the Central Universities (Grants No. WK2470000026 and No. WK2470000029). Z.-Q.Z. acknowledges the support from the Youth Innovation Promotion Association CAS.

APPENDIX A: WAVEGUIDE COUPLING AND LOSSES

The method of waveguide coupling is as follows. The output beam from the FC has a diameter of 2 mm. Three lenses modify the incoming and out-coupled beams as follows. The first two lenses have focal lengths of 100 and 150 mm respectively and a distance of 250 mm, forming a beam expander, which expands the beam diameter from 2 to 3 mm. The third 75-mm lens focuses the beam into the waveguide with the help of a three-axis translator. The focused beam has a diameter of approximately $10.9 \mu\text{m}$. By carefully adjusting the 75-mm lens, the diameter of the focused beam is modified to match the mode of the waveguide. After the waveguide, there are 75-, 150-, and 100-mm lenses in sequence to couple the laser into the FC.

The measurement of the insertion loss of the waveguide is implemented as follows. First, we carefully couple the laser into our waveguide, similar to that mentioned above but without the cryostat. To ensure the measured beam is actually guided in the waveguide, we check it in two ways. On the one hand, at the exit side of the waveguide, an aperture is placed between the 150-mm lens and 100-mm lens. The aperture is gradually closed until the single-mode coupling efficiency begins to decrease. A reflector is placed behind the out-coupled 100-mm lens to reflect the output beam of the waveguide onto a light plate by looking at the pattern on the light plate and adjusting the aperture so that only the guided mode can pass through. In our case, the power passing through the aperture is measured as 1.15 mW. After that, we remove the aperture and move the crystal to couple the laser into the bulk regime. The measured power is 1.21 mW after transmission. Finally, the insertion loss of the waveguide is calculated as $IL = -10 \times \log_{10} \frac{1.15}{1.21} = 0.22$ dB. The transmission loss is 0.15 dB/cm.

The transmission of the cryostat alone is 94.9%. The transmission of the bulk regime of the crystal is 82.7%, which is consistent with the calculated Fresnel loss ($\approx 16\%$ for YSO crystal under normal incidence). We note that here we assume that the Fresnel loss is the same for the waveguide and the bulk regime. However, the modified refractive index of the waveguide regime may lead to a different Fresnel loss in practice. As a result, the transmission loss may be underestimated here. The total transmission through the cryostat and the waveguide (bulk) regime of the crystal is 72.6% (77.6%). Therefore, the transmission of the waveguide alone is inferred to be 94%, i.e., insertion losses of 0.2 dB, which is consistent with the independently measured IL mentioned above. The transmission of the lenses that between the output window of the cryostat and the fiber coupler is 93.2%. The fiber coupling efficiency is 82.7%. The overall transmission efficiency from the front of the cryostat to the single-mode fiber is 56%.

APPENDIX B: THE ENERGY DIAGRAMS OF NINE CLASSES OF IONS OF $^{151}\text{Eu}^{3+}$ IN Y_2SiO_5 CRYSTAL

The aligned energy diagrams (Fig. 7) could help to understand the stick diagram in Fig. 2(b). For example, setting

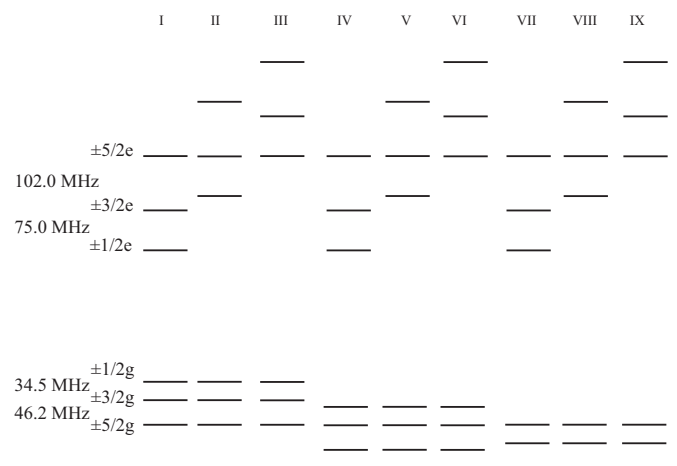


FIG. 7. The aligned energy diagrams of each class of ions.

the frequency of transition $|\pm 1/2\rangle_g \rightarrow |\pm 1/2\rangle_e$ of class-I ions as zero, the relative frequency of the transition $|\pm 3/2\rangle_g \rightarrow$

$|\pm 5/2\rangle_e$ of class-VIII ions is $34.5 + 46.2 + 34.5 + 102 + 75 + 102 = 394.2$ (MHz).

-
- [1] H. de Riedmatten, M. Afzelius, M. U. Staudt, C. Simon, and N. Gisin, *Nature (London)* **456**, 773 (2008).
- [2] N. Sangouard, C. Simon, H. de Riedmatten, and N. Gisin, *Rev. Mod. Phys.* **83**, 33 (2011).
- [3] T. Böttger, C. W. Thiel, R. L. Cone, and Y. Sun, *Phys. Rev. B* **79**, 115104 (2009).
- [4] M. Zhong, M. P. Hedges, R. L. Ahlefeldt, J. G. Bartholomew, S. E. Beavan, S. M. Wittig, J. J. Longdell, and M. J. Sellars, *Nature (London)* **517**, 177 (2015).
- [5] N. Sinclair, D. Oblak, C. W. Thiel, R. L. Cone, and W. Tittel, *Phys. Rev. Lett.* **118**, 100504 (2017).
- [6] C. Simon, H. de Riedmatten, M. Afzelius, N. Sangouard, H. Zbinden, and N. Gisin, *Phys. Rev. Lett.* **98**, 190503 (2007).
- [7] D. Lago-Rivera, S. Grandi, J. V. Rakonjac, A. Seri, and H. de Riedmatten, *Nature (London)* **594**, 37 (2021).
- [8] X. Liu, J. Hu, Z.-F. Li, X. Li, P.-Y. Li, P.-J. Liang, Z.-Q. Zhou, C.-F. Li, and G.-C. Guo, *Nature (London)* **594**, 41 (2021).
- [9] J. S. Tang, Z. Q. Zhou, Y. T. Wang, Y. L. Li, X. Liu, Y. L. Hua, Y. Zou, S. Wang, D. Y. He, G. Chen, Y. N. Sun, Y. Yu, M. F. Li, G. W. Zha, H. Q. Ni, Z. C. Niu, C. F. Li, and G. C. Guo, *Nat. Commun.* **6**, 8652 (2015).
- [10] M. Bonarota, J. Le Gouët, and T. Chaneliere, *New J. Phys.* **13**, 013013 (2011).
- [11] M. Businger, A. Tiranov, K. T. Kaczmarek, S. Welinski, Z. Zhang, A. Ferrier, P. Goldner, and M. Afzelius, *Phys. Rev. Lett.* **124**, 053606 (2020).
- [12] M. Afzelius, I. Usmani, A. Amari, B. Lauritzen, A. Walther, C. Simon, N. Sangouard, J. C. V. Minář, H. de Riedmatten, N. Gisin, and S. Kröll, *Phys. Rev. Lett.* **104**, 040503 (2010).
- [13] C. Laplane, P. Jobez, J. Etesse, N. Timoney, N. Gisin, and M. Afzelius, *New J. Phys.* **18**, 013006 (2015).
- [14] P. Jobez, C. Laplane, N. Timoney, N. Gisin, A. Ferrier, P. Goldner, and M. Afzelius, *Phys. Rev. Lett.* **114**, 230502 (2015).
- [15] M. Gündoğan, P. M. Ledingham, K. Kutluer, M. Mazzera, and H. de Riedmatten, *Phys. Rev. Lett.* **114**, 230501 (2015).
- [16] Y. Ma, Y.-Z. Ma, Z.-Q. Zhou, C.-F. Li, and G.-C. Guo, *Nat. Commun.* **12**, 2381 (2021).
- [17] P. Jobez, N. Timoney, C. Laplane, J. Etesse, A. Ferrier, P. Goldner, N. Gisin, and M. Afzelius, *Phys. Rev. A* **93**, 032327 (2016).
- [18] G. Corrielli, A. Seri, M. Mazzera, R. Osellame, and H. de Riedmatten, *Phys. Rev. Applied* **5**, 054013 (2016).
- [19] A. Seri, G. Corrielli, D. Lago-Rivera, A. Lenhard, H. de Riedmatten, R. Osellame, and M. Mazzera, *Optica* **5**, 934 (2018).
- [20] A. Seri, D. Lago-Rivera, A. Lenhard, G. Corrielli, R. Osellame, M. Mazzera, and H. de Riedmatten, *Phys. Rev. Lett.* **123**, 080502 (2019).
- [21] C. Liu, Z.-Q. Zhou, T.-X. Zhu, L. Zheng, M. Jin, X. Liu, P.-Y. Li, J.-Y. Huang, Y. Ma, T. Tu *et al.*, *Optica* **7**, 192 (2020).
- [22] T.-X. Zhu, C. Liu, L. Zheng, Z.-Q. Zhou, C.-F. Li, and G.-C. Guo, *Phys. Rev. Applied* **14**, 054071 (2020).
- [23] C. Liu, T.-X. Zhu, M.-X. Su, Y.-Z. Ma, Z.-Q. Zhou, C.-F. Li, and G.-C. Guo, *Phys. Rev. Lett.* **125**, 260504 (2020).
- [24] T. Zhong, J. M. Kindem, J. G. Bartholomew, J. Rochman, I. Craiciu, E. Miyazono, M. Bettinelli, E. Cavalli, V. Verma, S. W. Nam, F. Marsili, M. D. Shaw, A. D. Beyer, and A. Faraon, *Science* **357**, 1392 (2017).
- [25] I. Craiciu, M. Lei, J. Rochman, J. M. Kindem, J. G. Bartholomew, E. Miyazono, T. Zhong, N. Sinclair, and A. Faraon, *Phys. Rev. Applied* **12**, 024062 (2019).
- [26] J. M. Kindem, A. Ruskuc, J. G. Bartholomew, J. Rochman, Y. Q. Huan, and A. Faraon, *Nature (London)* **580**, 201 (2020).
- [27] M. U. Staudt, M. Afzelius, H. de Riedmatten, S. R. Hastings-Simon, C. Simon, R. Ricken, H. Suche, W. Sohler, and N. Gisin, *Phys. Rev. Lett.* **99**, 173602 (2007).
- [28] M. U. Staudt, S. R. Hastings-Simon, M. Nilsson, M. Afzelius, V. Scarani, R. Ricken, H. Suche, W. Sohler, W. Tittel, and N. Gisin, *Phys. Rev. Lett.* **98**, 113601 (2007).
- [29] E. Saglamyurek, N. Sinclair, J. Jin, J. A. Slater, D. Oblak, F. Bussières, M. George, R. Ricken, W. Sohler, and W. Tittel, *Nature (London)* **469**, 512 (2011).
- [30] N. Sinclair, E. Saglamyurek, H. Mallahzadeh, J. A. Slater, M. George, R. Ricken, M. P. Hedges, D. Oblak, C. Simon, W. Sohler, and W. Tittel, *Phys. Rev. Lett.* **113**, 053603 (2014).
- [31] M. F. Askarani, M. G. Puigibert, T. Lutz, V. B. Verma, M. D. Shaw, S. W. Nam, N. Sinclair, D. Oblak, and W. Tittel, *Phys. Rev. Applied* **11**, 054056 (2019).
- [32] E. Saglamyurek, M. G. Puigibert, Q. Zhou, L. Giner, F. Marsili, V. B. Verma, S. W. Nam, L. Oesterling, D. Nippa, D. Oblak *et al.*, *Nat. Commun.* **7**, 11202 (2016).
- [33] J. Jin, E. Saglamyurek, M. G. Puigibert, V. Verma, F. Marsili, S. W. Nam, D. Oblak, and W. Tittel, *Phys. Rev. Lett.* **115**, 140501 (2015).
- [34] F. Chen and J. R. V. de Aldana, *Laser Photon. Rev.* **8**, 251 (2014).
- [35] B. Lauritzen, N. Timoney, N. Gisin, M. Afzelius, H. de Riedmatten, Y. Sun, R. M. Macfarlane, and R. L. Cone, *Phys. Rev. B* **85**, 115111 (2012).
- [36] M. Afzelius, C. Simon, H. de Riedmatten, and N. Gisin, *Phys. Rev. A* **79**, 052329 (2009).
- [37] M. Bonarota, J. Ruggiero, J.-L. Le Gouët, and T. Chanelière, *Phys. Rev. A* **81**, 033803 (2010).
- [38] N. Timoney, B. Lauritzen, I. Usmani, M. Afzelius, and N. Gisin, *J. Phys. B: At. Mol. Opt. Phys.* **45**, 124001 (2012).
- [39] M. Gündoğan, M. Mazzera, P. M. Ledingham, M. Cristiani, and H. de Riedmatten, *New J. Phys.* **15**, 045012 (2013).
- [40] A. Arcangeli, M. Lovrić, B. Tumino, A. Ferrier, and P. Goldner, *Phys. Rev. B* **89**, 184305 (2014).
- [41] M. Lovrić, P. Glasenapp, D. Suter, B. Tumino, A. Ferrier, P. Goldner, M. Sabooni, L. Rippe, and S. Kröll, *Phys. Rev. B* **84**, 104417 (2011).
- [42] A. Holzäpfel, J. Etesse, K. T. Kaczmarek, A. Tiranov, N. Gisin, and M. Afzelius, *New J. Phys.* **22**, 063009 (2020).
- [43] P. Jobez, I. Usmani, N. Timoney, C. Laplane, N. Gisin, and M. Afzelius, *New J. Phys.* **16**, 083005 (2014).